Numerical Modelling of Fluid-Structure Interaction for Thermal Buckling in Hypersonic Flow

Katharina Martin, Dennis Daub, Burkard Esser, Ali Gülhan, and Stefanie Reese

Abstract Experiments have shown that a high-enthalpy flow field might lead under certain mechanical constraints to buckling effects and plastic deformation. The panel buckling into the flow changes the flow field causing locally increased heating which in turn affects the panel deformation. The temperature increase due to aerothermal heating in the hypersonic flow causes the metallic panel to buckle into the flow. To investigate these phenomena numerically, a thermomechanical simulation of a fluid-structure interaction (FSI) model for thermal buckling is presented. The FSI simulation is set up in a staggered scheme and split into a thermal solid, a mechanical solid and a fluid computation. The structural solver *Abaqus* and the fluid solver *TAU* from the German Aerospace Center (DLR) are coupled within the FSI code *ifls* developed at the Institute of Aircraft Design and Lightweight Structures (IFL) at TU Braunschweig. The FSI setup focuses on the choice of an equilibrium iteration method, the time integration and the data transfer between grids. To model the complex material behaviour of the structure, a viscoplastic material model with linear isotropic hardening and thermal expansion including material parameters, which are nonlinearly dependent on temperature, is used.

K. Martin (✉) · S. Reese
Institute of Applied Mechanics, RWTH Aachen University,
Mies-van-der-Rohe-Str. 1, 52074 Aachen, Germany
e-mail: katharina.martin@rwth-aachen.de

S. Reese
e-mail: stefanie.reese@rwth-aachen.de

D. Daub · B. Esser · A. Gülhan
Supersonic and Hypersonic Technology Department, German Aerospace Center (DLR), Institute of Aerodynamics and Flow Technology, Köln, Germany
e-mail: dennis.daub@dlr.de

B. Esser
e-mail: burkard.esser@dlr.de

A. Gülhan
e-mail: ali.guelhan@dlr.de

© The Author(s) 2021

N. A. Adams et al. (eds.), *Future Space-Transport-System Components under High Thermal and Mechanical Loads*, Notes on Numerical Fluid Mechanics and Multidisciplinary Design 146, https://doi.org/10.1007/978-3-030-53847-7_22

1 Introduction

Thermal buckling is a key issue at the wing leading edge of aeroplanes and reusable launch vehicles [11, 12, 25] which leads to a stiffness reduction [25]. Buckles were also observed over much of the underside of the experimental aircraft Y-12 [24]. Thermal buckling occurs under thermal loads combined with unavoidable constraints, which prevent the movement of the structure. First investigations of thermal buckling were conducted by [1, 26]. The phenomenon is particularly significant in hypersonic flow [9, 20] because of the strong interdependence between flow field and structure. Due to the buckling of the structure, shocks and expansion regions occur along the panel, which lead to a change in temperature, pressure and velocity of the fluid, which in turn alters the structural deformation. This can decrease the efficiency or even lead to structural failure. The effects of thermal buckling are shown in Fig. 1. Thermal buckling was shown in the experiments conducted by [2, 6]. A metallic panel was mounted to a support structure and its movement is restricted at the connections. The panel buckling is investigated at a Mach number of $\mathrm{Ma} = 7.7$ in a wind tunnel. Thermal loads lead to an expansion of the panel, which causes it to buckle into the flow.

Numerical investigations of coupled fluid structure interaction of different deformed and undeformed rigid panels at hypersonic speed ($\mathrm{Ma} = 11.44$) were conducted by [12]. In their consequent work, deformations caused by thermal heating were included [11]. Fluid-thermal-structural interaction at hypersonic speed ($\mathrm{Ma} = 5.3$) with cyclic loading including dynamic effects due to fluttering of skin panels, damage fatigue and effects of strain hardening and its comparison to elastic models were investigated in [14]. A thermoviscoplastic analysis of cooled structures in hypersonic flow was conducted by [27]. Experimental validation of numerical FSI in hypersonic flow was investigated by [17, 30, 31]. In the latter papers, only thermal aspects in the structural investigation were taken into account.

In this work, the simulation of a thermomechanical fluid-structure interaction of thermal buckling is investigated and compared to experimental results conducted by [6]. The experimental results show the largest increase in deformation of about 12 mm in the first 60 s. The change in deformation is generally slow. Therefore, no dynamical effects are considered and a steady state is assumed for the fluid and structural computation, which means that an equilibrium between structure and fluid must be obtained for each time step. For the fluid computation the fluid solver *TAU* developed at the German Aerospace Center (DLR) is used [16]. The structural computation is divided into a transient thermal and a static mechanical analysis. Results from the fluid computation are used as boundary conditions and loads for the structural analysis, and vice versa. For the structural material a viscoplastic model including large deformations [29] and thermal expansions is chosen. A highly temperature- and rate-dependent material behaviour must be considered since the temperature ranges from room temperature up to 1200 °C and viscous effects play an important role at temperatures above 600 °C for the chosen material [10]. This is achieved by defining material parameters which are nonlinearly dependent on the temperature [21, 28] and a material model, which includes viscous effects. Therefore, a thermodynamically

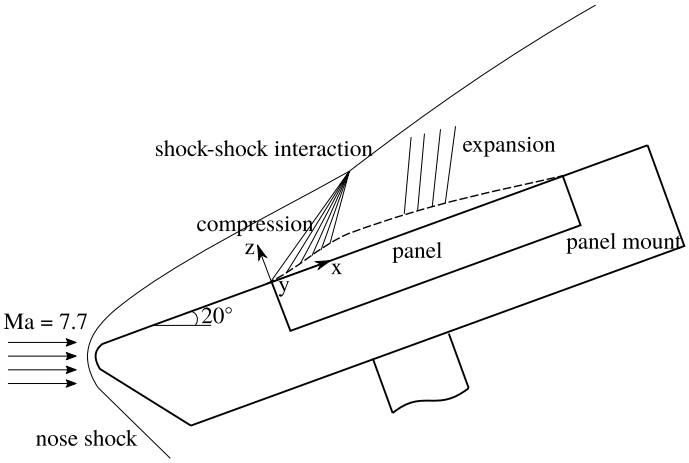

Fig. 1 Influence of thermal buckling on fluid flow

consistent model of viscoplasticity with linear isotropic hardening for large deformations is chosen, which is based on [7, 15, 29]. This material model is implemented as a User Material Subroutine (UMAT) into the commercial finite element program *Abaqus*. The transient thermal computation includes heat conduction and radiation on the panel coupling interface and in the cavity between panel and its mount. The fluid and structural computation are coupled by the FSI coupling tool *ifls* which is provided by the IFL at TU Braunschweig. The software implementation of the FSI is done by [8, 13, 20].

2 Fluid-Structure Interaction

ifls provides a coupling interface for several structural and fluid solvers, which are easily exchangeable. For this computation the structural solver *Abaqus FEA* and the fluid solver *TAU* are used. In Fig. 2 the coupling scheme for the buckling problem is shown. Bold arrows denote the flow of the diagram. It is a sequential coupling scheme with three parts

- thermal structural computation in Abaqus FEA,
- mechanical structural computation in Abaqus FEA with an implemented user material model,
- fluid computation,

Between each computation a step is interposed in which the state quantities used as boundary conditions for the following computation are transferred. Quantities denoted by $(\cdot)_f$ are input and output values of the fluid computation; quantities denoted by $(\cdot)_s$ are those of the structural computation. Since the maximum defor-

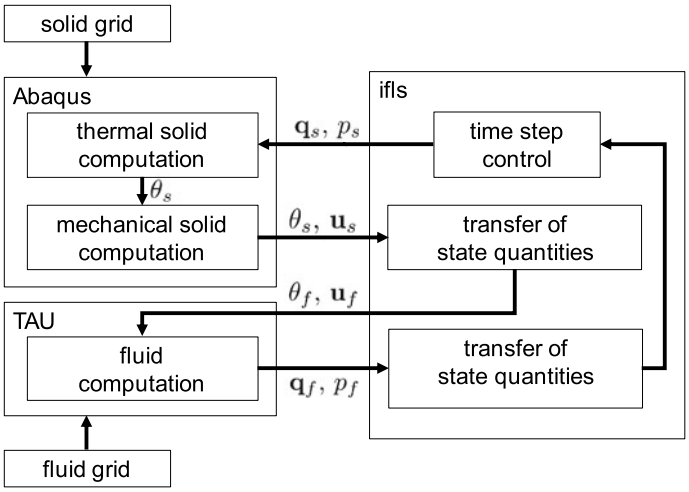

Fig. 2 Staggered coupling scheme of *ifls* [8, 13, 20]

mation of the panel of 12 mm takes 60 s to fully develop, it is rather slow. Therefore, an equilibrium state for fluid and solid can be assumed in each time step. For this, a Dirichlet–Neumann method is used. The Dirichlet problem is solved in the fluid computation with the displacement $\mathbf{u}_f$ and the temperature θ_f at the boundaries. The Neumann problem is solved in both structural computations. The boundary condition for the thermal solid computation is the heat flux $\mathbf{q}_s$ from the fluid computation. The calculated temperature θ_s and the pressure p_s are used as boundary conditions for the mechanical solid computation. The convergence criterion for the equilibrium method is the Aitken method, which improves the rate of convergence. For the time integration, an iterative staggered procedure is used as shown in [9]. Due to the fact that the meshes are non-conforming, the mentioned state quantities, e.g. results from both computations must be transferred from one grid to the other. This is done by means of a Lagrange multiplier and a coupling matrix which defines the explicit relations between fluid and solid mesh [9]. No remeshing of the fluid mesh is needed due to a mesh adaptation where the fluid mesh is moved with the deformation of the panel and the resultant shock form changes [20].

3 Structural Model

The structural computation is divided into a transient thermal and a static mechanical analysis. The structural model is shown in Fig. 3. The frame and the panel, shown in blue and brown, are made out of Incoloy 800 HT. For the isolation, shown in green, white and red, Schupp Ultra Board 1850/500 by Schupp Industriekeramik is used. The support plate is made out of Copper and is shown in grey. The rounded nose,

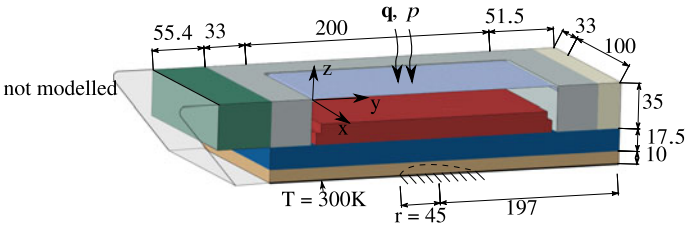

Fig. 3 Thermal and mechanical boundary conditions (BC) for structural model: circular fixation and isothermal BC on support plate, pressure and heat flux on top surface (all dimensions in *mm*)

which can be seen in the figure, is not modelled in the structural computation. Since the isolation is located between the rounded nose and the frame, the authors assume that it will not have an influence on the temperature distribution and displacement of the model. To reduce computational time symmetry is exploited and only half of the structure is considered. Shell elements are used for the panel and continuum elements for the isolation and frame, respectively. Finite elements based on reduced integration with hourglass stabilization are used for the spatial discretization [19].

3.1 Thermal Analysis

For the thermal analysis a standard transient *Abaqus* heat transfer and radiation model is used. The implemented energy balance is

$$\int_V \rho\, \dot{e}\, \mathrm{d}V = \int_S \mathbf{q} \cdot \mathrm{d}S + \int_V r\, \mathrm{d}V \tag{1}$$

with the volume V and surface S of the solid material, the density ρ, the rate of the internal energy $\dot{e}$, the heat flux q and the heat r supplied externally into the body. For a purely thermal analysis, the internal energy is only dependent on the temperature $e = e(\theta)$. Heat conductivity is given by Fourier's law $\mathbf{q} = -\lambda \frac{\partial \theta}{\partial \mathbf{x}}$ with the conductivity λ and the position vector $\mathbf{x}$. On the top surface of the structure a radiation boundary condition is applied given by $q_r = \varepsilon \left(\theta^4 - \theta_\infty^4\right)$, with the emissivity ε and the sink temperature θ_∞.

The three-dimensional thermal model is composed of 43760 DC3D8 and 2593 DS4 elements with eleven integration points over the thickness. The boundary conditions are taken from the experiments. The temperature at the bottom of the panel is held fixed at $T = 300\,\mathrm{K}$ due to a water-cooled support plate, the heat flux from the fluid computation is applied to the top surface. A surface radiation boundary condition is used at the top surface. Cavity radiation occurs in the cavity between panel, frame and the insulation. The emissivity is 0.8 for Incoloy 800 HT [18] and 0.3 for the insulation [6]. The emissivity of Incoloy 800 HT was investigated at tem-

peratures of 800 and 1100 °C and were found to be constant. Cooling of the panel is caused by heat radiation from the panel to the surrounding structures and the flow. The temperature dependent material parameters thermal conductivity, specific heat, thermal expansion and density can be found in [20, 23].

3.2 Structural Analysis

For the mechanical analysis a standard static *Abaqus* material model for linear elasticity with thermal expansion is used for the insulation. For the Incoloy a static elasto-viscoplastic material model with linear isotropic hardening and thermal expansion is implemented in an *Abaqus* UMAT. A multiplicative split is used for the deformation gradient $\mathbf{F} = \mathbf{F}_e \, \mathbf{F}_p$. $\mathbf{F}_e$ represents the elastic part and $\mathbf{F}_p$ is the plastic part due to dislocation of the crystal grid. The constitutive equations are derived with the Clausius–Duhem inequality for isothermal processes

$$-\dot{\Psi} + \boldsymbol{\tau} \cdot \mathbf{d} \geq 0 \tag{2}$$

Here, $\dot{\Psi}$ denotes the rate of the Helmholtz free energy, $\boldsymbol{\tau}$ the Kirchhoff stress tensor, $\mathbf{d}$ the symmetric part of the velocity gradient $\mathbf{l} = \dot{\mathbf{F}}\mathbf{F}^{-1}$. The Helmholtz free energy Ψ depends on the elastic Green-Lagrange strain tensor $\mathbf{E}_e$, on the accumulated plastic strain variable κ and the temperature θ. It is additively split into an elastic, an isotropic hardening and a thermal expansion part:

$$\begin{aligned} \Psi &= \Psi_e(\mathbf{E}_e) + \Psi_{iso}(\kappa) + \Psi_{th}(\theta) \\ &= \frac{\lambda}{2}[\mathrm{tr}(\mathbf{E}_e)]^2 + \mu \, \mathrm{tr}\,(\mathbf{E}_e^2) + H\kappa - (\theta - \theta_0)\, \alpha_T \, \lambda \, \det(\mathbf{F}) \end{aligned} \tag{3}$$

The elastic Green-Lagrange strain tensor is calculated by $\mathbf{E}_e = \frac{1}{2}(\mathbf{C}_e - \mathbf{I})$, whereas $\mathbf{C}_e$ is the right Cauchy–Green tensor and $\mathbf{I}$ the identity matrix. μ and λ are the Lame constants given by the Young's modulus and the Poisson's ratio. H is the hardening parameter and α_T the thermal expansion parameter. Inserting Eq. (3) into the Clausius–Duhem equation (2), the Kirchhoff stress tensor $\boldsymbol{\tau}$ and the hardening variable q are derived, c.f. [22]:

$$\boldsymbol{\tau} = 2\mathbf{F}_e \frac{\partial \Psi_e}{\partial \mathbf{C}_e} \mathbf{F}_e^T, \qquad q = -\frac{\partial \Psi}{\partial \kappa} \tag{4}$$

The thermodynamical consistency is fulfilled with the evolution equations

$$\mathbf{d}_p = \dot{\lambda} \frac{\partial \Phi}{\partial \boldsymbol{\tau}}, \qquad \dot{\kappa} = \dot{\lambda} \frac{\partial \Phi}{\partial q} \tag{5}$$

Here, $\mathbf{d}_p$ is the symmetric part of the plastic velocity gradient $\mathbf{l}_p$ and Φ is the von-Mises yield surface

$$\Phi = ||\text{dev}\boldsymbol{\tau}|| - \sqrt{\frac{2}{3}}(\tau_y - q) \tag{6}$$

The plastic multiplier

$$\dot{\lambda} = \frac{\bar{\Phi}}{\eta} \tag{7}$$

completes the set of equations with the normalized yield function $\bar{\Phi}$. η is the viscosity parameter, which controls the rate dependency of the material. The material model is modified for a plane stress state in order to also use it for shell elements. The structural model with the boundary conditions and element description is shown in Fig. 3. For the mechanical boundary conditions, the nodes at the circular clamping are fixed and the temperature distribution over the whole structure is given from the thermal analysis. The pressure of the fluid is given on the top surface. The three-dimensional mechanical model is composed of 43760 C3D8R and 2593 S4R elements with eleven integration points over the thickness. Mechanical material tests were conducted at the *Institute of Applied Mechanics* to determine the Young's modulus E, the yield stress τ_y and the linear hardening parameter H over a temperature range of 20–1000 °C. The results can be found in Table 1. The Poisson's ratio and the viscosity parameter are taken from [20].

Table 1 Temperature dependent material parameters for the mechanical analysis

Temperature	Young's modulus (GPa)	Yield stress (MPa)	Hardening parameter (MPa)
20	197	220	662
100	191	209	685
200	185	178	714
300	178	150	731
400	170	127	748
500	165	110	766
600	158	112	706
700	150	114	601
800	139	109	300
900	134	100	45
1000	127	82	2

4 Fluid Model

The fluid computation is performed by means of the program *TAU* from the DLR [17]. For the fluid simulation, a laminar solver is used. For the spatial discretization the AUSMDV-Upwind method is used and for the time integration a pseudo 3rd-order Runge-Kutta method. The freestream conditions for the fluid computation, which have also been used for the experiments [3], are given in Table 2. An ideal gas law is used. Chemical non-equilibrium is not considered. The boundary conditions along the domain are shown in Fig. 4. The fluid grid has local refinements at the expected shock interface of the detached bow shock, at the boundary layer and at the region where isotropic compression occurs. Only the flow across the panel and frame is simulated, the flow around the structure is not considered. Results from [20] suggest that it might have an influence on the temperature distribution of the panel and will be investigated in the future. To reduce the computational time, symmetry is exploited and only half of the flow is simulated.

Table 2 Freestream conditions [3]

Ma_∞	T_∞	p_∞	Pr	γ	R
7.7	477 K	50.3 Pa	0.72	1.451	340.8 J/(kg K)

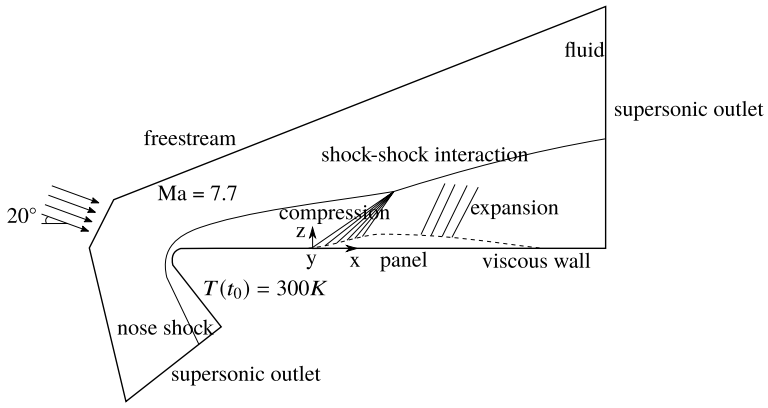

Fig. 4 Boundary conditions of fluid flow

5 Results

5.1 Solid

In Fig. 5 (left) the deformation of the experiment [2, 5] and simulation is compared at the *center* locations over the simulation time of 120 s. The coordinates of this and all other used locations are given in Table 3.

The calculated deformation in the *center* is in very good agreement with the experimental results of all runs, for which always a new panel was used. The maximum amplitude as well as the development over the time coincides with all experimental investigations. The decrease in deformation after about 70 s, which is visible in the experimental results, is explained by the thermal expansion of the frame, which yields to an overall decrease of the amplitude. It is not as developed in the simulation and takes place at a later stage, at 110 s. In Fig. 5 (right) the deformation is compared at all measured positions with the experimental results of *run 5*. All four simulated curves are in good agreement for the first 10–20 s. Afterwards the positions *front* and *center* lag behind the experimental results, however exceed the deformations after about 50–60 s. The deformation at the *left* are lower between 20 and 70 s, however are in very good agreement before and afterwards. The deformations at the *rear* are

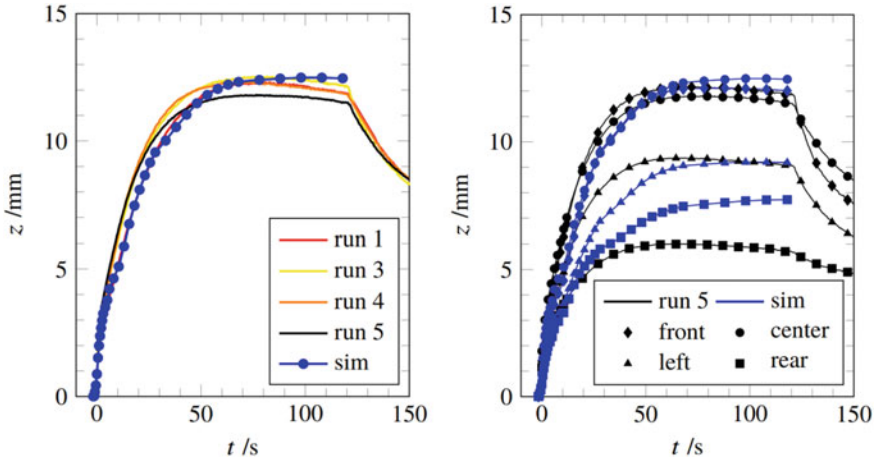

Fig. 5 Comparison of the displacement over time of simulation and experiment—**Left**: all *center* position. **Right**: all positions compared with experiment (run 5)

Table 3 Measurement positions [3]

Position	Front	Left	Center	Rear
x (mm)	50	100	100	150
y (mm)	0	−50	0	0

in good agreement until 30 s and are higher afterwards. The deformation at the *center* are overestimated by about 0.8 mm at 120 s compared to the experimental results of *run 5*; the *front* and *left* differ by only 0.1 mm at 120 s. However, the deformation at the *rear* is 2 mm higher than in the experiments. As already shown the experimental results for the different runs differ by about 0.8 mm as well. Therefore, a difference of about 0.8 mm is considered a good agreement with the experimental results. In Fig. 6 (left) the temperature distribution over time at the *center* point is shown and the calculated temperature is 50 K lower than the experimental results. The slopes of the temperature are consistent for experiment and simulation for the considered time period. This suggests that the heat transfer from the fluid to the structural heat computation is correctly modelled. The temperature in the first 40 s is about 70 K lower compared to the experimental results. A temperature deviation between the four experimental runs of about 50 K is observed. The temperature at the four positions is compared to *run 5* of the experiments in Fig. 6 (right) [2]. As it has been shown for the deformation, the calculated temperature is also lower than the experimentally determined temperature in first 40–50 s. Only for the *rear* it exceeds it afterwards. For the positions *center, left* and *rear* the temperatures lie within the uncertainty of the measurement and are considered to be in good agreement. The temperature at the *front* is 150 K lower than in the experiment at 120 s. Also the slopes of the temperature are in good agreement for all positions except for the *front*. At this position the temperature increases only slightly after 50 s. As for now only an ideal gas law is used for the fluid computation. Catalytical effects might have an influence of the temperature, which is to be investigated. The displacement contour and form of the buckle is compared in Fig. 7 with the experimental results at $t = 60$ s. Both contour plots show a wavy form with the highest amplitude shifted towards small x-values, i.e. shifted towards the inflow. The position of the highest amplitude of the simulation and the deformation at the centreline is in very good agreement with the experimental results. Merely, the slope at values larger than $x = 100$ differs slightly. A buckling into the corners, which is shown in the experimental contour plot, was not achieved in the simulations. An investigation of different boundary conditions at the connection between panel and frame did not lead to an increase of amplitude of the corners of the panel. This needs to be further investigated. The temperature contour plots for simulation and experiment are shown in Fig. 8 at $t = 60$ s. The temperature distributions differ especially at the front of the panel. A steeper increase of the temperature slope is shown in the experimental results compared to the simulation. A temperature of 1200 K is present at $x = 10$ mm in the experiments compared to $x = 30$ mm in the simulation. At values larger than $x = 100$ mm, the temperature coincides at the centerline. The temperature isoline of 1200 K in the experiments extends into the front corners and into the back corners for the 1000 K isoline. This is not observed in the simulation as the corners do not buckle, hence a temperature increase at these locations is not possible.

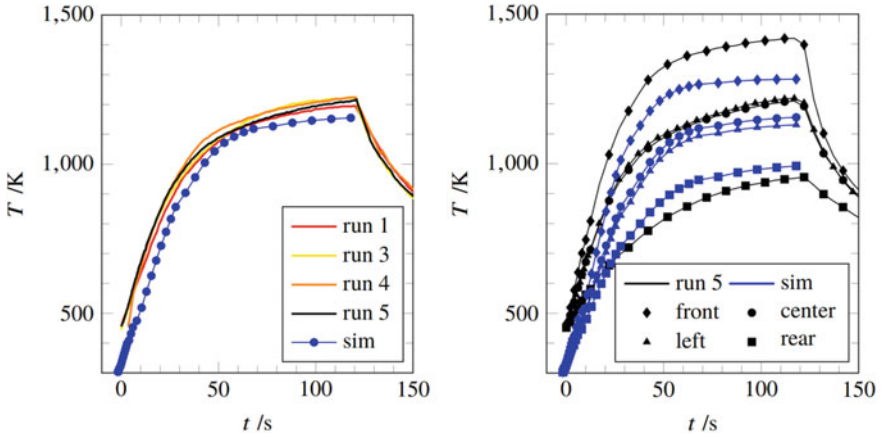

Fig. 6 Comparison of the temperature over time of simulation and experiment—**Left**: all *center* position. **Right**: all positions compared with experiment (run 5)

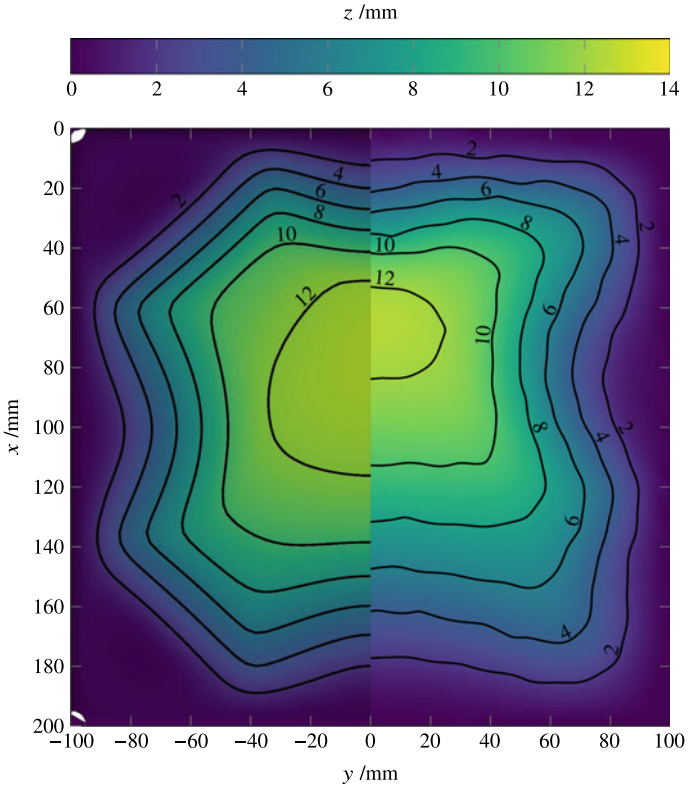

Fig. 7 Displacement contour plot at t = 60 s; left: simulation, right: experiment [2, 4]

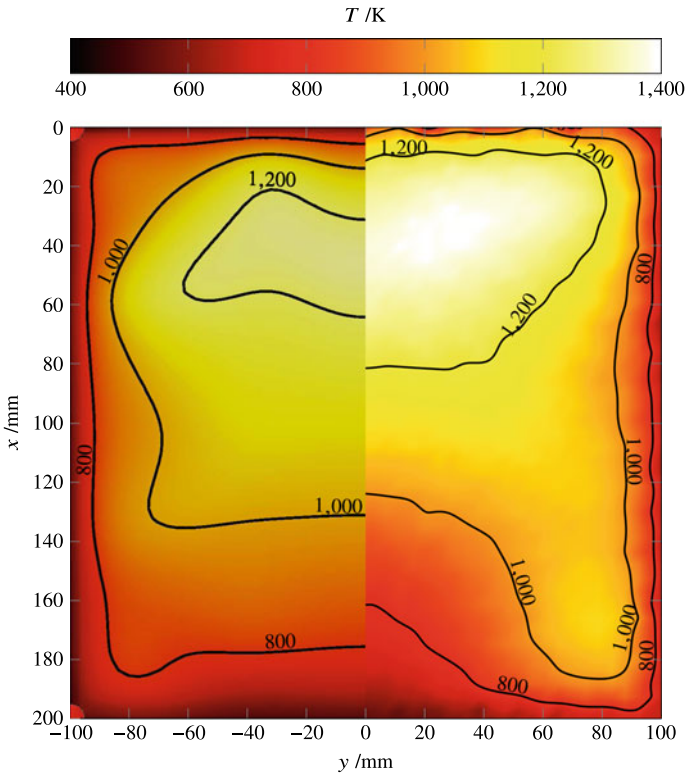

Fig. 8 Temperature contour plot at t = 60 s; left: simulation, right: experiment [2, 4]

5.2 *Fluid*

The computational results from the fluid calculation are evaluated quantitatively. The Mach number Ma is shown in Fig. 9 for the times $t = 0\,\text{s}$, $t = 30\,\text{s}$, $t = 60\,\text{s}$ and $t = 120\,\text{s}$. At $t = 0\,\text{s}$ the panel is undeformed. A detached bow is located at the nose, which causes a drop of the Mach number over the bow shock. The Mach number at the boundary is zero. At $t = 30\,\text{s}$ the panel heats up and therefore buckles into the flow. The compression region in the front of the panel can be seen. This shock interacts with the detached bow shock and causes an expansion of shock. At the maximum buckling amplitude a Prandtl-Meyer expansion begins, where the fluid accelerates and the pressure decreases. At $t = 60\,\text{s}$ the shock regions have reached their maximum due to the maximum deformation at that time. At $t = 120\,\text{s}$ the fluid flow field has not changed due to a constant temperature and deformation of the panel.

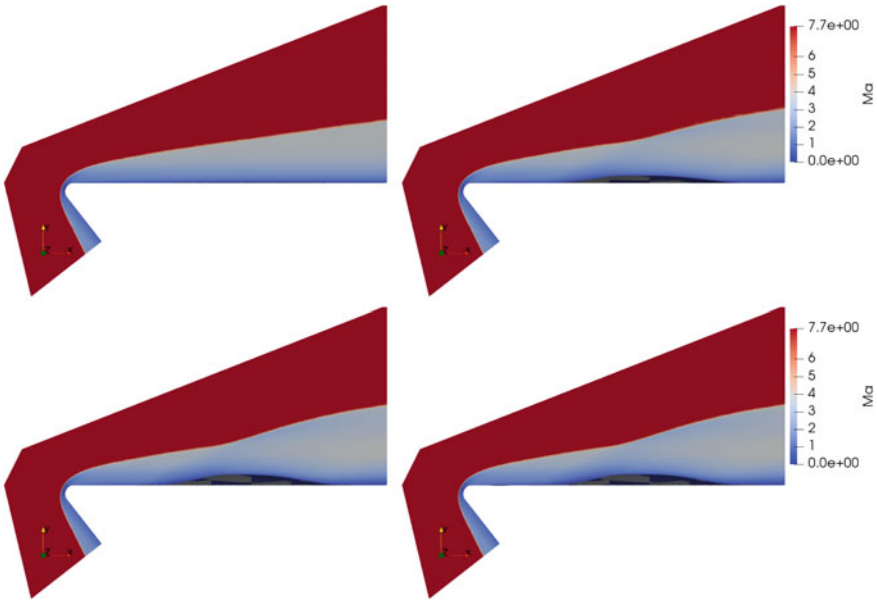

Fig. 9 Mach number at $t = 0$ s (top left), $t = 30$ s (top right), $t = 60$ s (bottom left) and $t = 120$ s (bottom right); max = 7.7

6 Conclusion

In this work, a simulation of a thermomechanical fluid-structure interaction for thermal buckling in hypersonic flow was presented. The fluid-structure interaction is divided into a transient thermal and a static mechanical structural analysis and a fluid simulation. For the static analysis a viscoplastic material with linear isotropic hardening for finite strains and thermal expansion including temperature dependent material parameters was implemented in *Abaqus* as a UMAT. For the fluid computation the fluid solver *TAU* was used. Both programs are loosely coupled by the FSI coupling tool *ifls*. Displacement and temperature results from the simulation were compared with experimental data. The buckling form of the panel coincides with the experimental results except for the corners. If this effect is caused by the boundary conditions will be investigated in future. Furthermore, the maximum displacements at the *front, center* and *left* from the simulation conform with the experimental results within the uncertainty of the repeatability. Deformations at the *rear* deviate after 40 s. The temperatures at all positions except the *rear* are lower than the experimental determined temperatures. The results of the fluid computation are evaluated qualitatively and show the expected behaviour. In future works the effects of the flow around the panel should be should be investigated. Since catalytic effects are difficult to be determined in the experiments, the influence can only be estimated. An

investigation if there are deviations compared to the ideal gas solution and if those will lead to an increase in temperature will be investigated in future.

Acknowledgements Financial support has been provided by the German Research Foundation (Deutsche Forschungsgemeinschaft – DFG) in the framework of the Sonderforschungsbereich Transregio 40.

References

1. Culler, A., McNamara, J.: Impact of fluid-thermal-structural coupling on response preduction of hypersonic skin panels. Amer. Inst. Aeronaut. Astronaut. J. **49**, 2393–2406 (2011)
2. Daub, D., Esser, B., Gülhan, A.: Experiments on high temperature hypersonic fluid-structure interaction with plastic deformation. AIAA J. (in press) (2020)
3. Daub, D., Esser, B., Willems, S., Gülhan, A.: Experimental studies on aerothermal fluid-structure interaction with plastic deformation. SFB TRR40 Annual Report 2018, pp. 269–279 (2018)
4. Daub, D., Esser, B., Willems, S., Gülhan, A.: Experimental studies on aerothermal fluid-structure interaction with plastic deformation. SFB TRR40 Annual Report 2018, pp. 269–279 (2019)
5. Daub, D., Esser, B., Willems, S., Gülhan, A.: Experiments on aerothermal supersonic fluid-structure interaction. SFB TRR40 Final Report 2020 (2020)
6. Daub, D., Esser, B., Willems, S., Gülhan, A.: Experiments on thermomechanical fluid-structure interaction in supersonic flows. SFB TRR40 Annual Report 2017, pp. 243–254 (2017)
7. Dettmer, W., Reese, S.: On the theoretical and numerical modelling of Armstrong-Frederick kinematic hardening in the finite strain regime. Comput. Methods Appl. Mech. Eng. **193**, 87–116 (2004)
8. Haupt, M., Niesner, R., Unger, R., Horst, R.: Model configuration for the validation of aerothermodynamic thermal-mechanical fluid-structure interactions. In: Proceedings of the ASME 11th Biennial Conference on Engineering Systems Design and Analysis (ESDA2012) (2004). Nantes, France
9. Haupt, M., Niesner, R., Unger, R., Horst, P.: Coupling techniques for thermal and mechanical fluid-structure-interactions in aeronautics. PAMM **5**(1), 19–22 (2005). https://doi.org/10.1002/pamm.200510006
10. Hollstein, T., Voss, B.: Experimental Determination of the High-Temperature Crack Growth Behavior of Incoloy 800H. In: Nonlinear Fracture Mechanics: Volume I - Time-Dependent Fracture, ASTM STP 995, vol. 1, pp. 195–213 (1989)
11. Kontinos, D.A., Palmer, G.: Numerical simulation of metallic thermal protection system panel bowing. J. Spacecr. Rockets **36**(6), 842–849 (1999). https://doi.org/10.2514/2.3523
12. Kontinos, D.: Coupled thermal analysis method with application to metallic thermal protection panels. J. Thermophys. Heat Transfer **11**(2), 173–181 (1997). https://doi.org/10.2514/2.6249
13. Kowollik, D., Tini, V., Reese, S., Haupt, M.: 3D fluid-structure interaction analysis of a typical liquid rocket engine cycle based on a novel viscoplastic damage model. Int. J. Numer. Methods Eng. **94**, 1165–1190 (2013). https://doi.org/10.1002/nme.4488
14. LaFontaine, J.H., Gogulapati, A., McNamara, J.J.: Effects of strain hardening on response of skin panels in hypersonic flow. AIAA J. **54**(6), 1974–1986 (2016). https://doi.org/10.2514/1.J054582
15. Lion, A.: Constitutive modelling in finite thermoviscoplasticity: a physical approach based on nonlinear rheological models. Int. J. Plast. **16**, 469–494 (2000)
16. Mack, A., Hannemann, V.: Validation of the unstructured DLR-TAU-Code for hypersonic flows. https://doi.org/10.2514/6.2002-3111. https://arc.aiaa.org/doi/abs/10.2514/6.2002-3111

17. Mack, A., Schaefer, R.: Fluid structure interaction on a generic body-flap model in hypersonic flow. J. Spacecr. Rockets **42**(5), 769–779 (2005). https://doi.org/10.2514/1.13001
18. Martin, K., Reese, S.: Numerical modelling of thermal buckling. SFB TRR40 Annual Report 2017, pp. 291–301 (2018)
19. Martin, K., Reese, S.: Thermo-mechanical fluid-structure interaction for thermal buckling. PAMM **19**(1), e201900,456 (2019). https://doi.org/10.1002/pamm.201900456. https://onlinelibrary.wiley.com/doi/abs/10.1002/pamm.201900456
20. Niesner, R.: Gekoppelte Simulation thermisch-mechanischer Fluid-Struktur-Interaktion für Hyperschall-Anwendungen. Ph.D. thesis, Technische Universität Carolo-Wilhelmina zu Braunschweig (2008)
21. Nowinski, J. (ed.): Theory of Thermoelasticity with Applications. Springer, Netherlands (1978)
22. Reese, S., Wriggers, P.: A material model for rubber-like polymers exhibiting plastic deformation: computational aspects and a comparison with experimental results. Comput. Methods Appl. Mech. Eng. **148**, 279–298 (1997)
23. Special Metals Wiggin Limited: Incoloy alloy 800H and 800HT. www.specialmetals.com (2004)
24. Spottswood, S., Beberniss, T., Eason, T., Perez, R., Donbar, J., Ehrhardt, D., Riley, Z.: Exploring the response of a thin, flexible panel to shock-turbulent boundary-layer interactions. J. Sound Vib. **443** (2018). https://doi.org/10.1016/j.jsv.2018.11.035
25. Stillwell, W.H.: X-15 Research Results -. Scientific and Technical Information Division, National Aeronautics and Space Administration (1965)
26. Thornton, E., Dechaumphai, P.: Coupled flow, thermal, and structural analysis of aerodynamically heated panels. J. Aircr. **25**, 1052–1059 (1988)
27. Thornton, E., Oden, J., Tworzydlo, W., Youn, S.K.: Thermoviscoplastic analysis of hypersonic structures subjected to severe aerodynamic heating. J. Aircr. - J AIRCRAFT **27**, 826–835 (1990). https://doi.org/10.2514/3.45943
28. Treloar, L. (ed.): The Physics of Rubber Elasticity. Oxford University Press, USA (1975)
29. Vladimirov, I., Pietryga, M., Reese, S.: On the modelling of non-linear kinematic hardening at finite strains with application to springback - Comparison of time integration algorithms. Int. J. Numer. Methods Eng. **75**, 1–28 (2007)
30. Willems, S., Esser, B., Gülhan, A.: Experimental and numerical investigation on thermal fluid-structure interaction on ceramic plates in high enthalpy flow. CEAS Space J. **7** (2015). https://doi.org/10.1007/s12567-015-0101-5
31. Willems, S.: Strömungs-Struktur-Wechselwirkung in Überschallströmungen. Ph.D. thesis, DLR/RWTH Aachen University (2017). https://elib.dlr.de/116735

Open Access This chapter is licensed under the terms of the Creative Commons Attribution 4.0 International License (http://creativecommons.org/licenses/by/4.0/), which permits use, sharing, adaptation, distribution and reproduction in any medium or format, as long as you give appropriate credit to the original author(s) and the source, provide a link to the Creative Commons license and indicate if changes were made.

The images or other third party material in this chapter are included in the chapter's Creative Commons license, unless indicated otherwise in a credit line to the material. If material is not included in the chapter's Creative Commons license and your intended use is not permitted by statutory regulation or exceeds the permitted use, you will need to obtain permission directly from the copyright holder.